Chapter 4: Morphology characterisation

4.1 Introduction

We have observed that the time-evolution of heat in the Nanocor-based systems is faster than those which are based on Nanoblend, implying that the crystallisation process is faster in the former. In this chapter, the final morphologies are studied in order to investigate the consequences of this. Although the crystallisation behaviour of the Nanoblend-based systems was very subtle, the presence of lamellar thickening suggested that a certain amount of lamellar disruption was taking place. It therefore behoves us to examine the consequences of the crystallisation kinetics on the superlamellar morphologies of both Nanocor- and Nanoblend-based materials. Furthermore, we will see in this chapter that although the differences in particle size distribution between the masterbatches extend to low magnifications, the spatial distribution is essentially uniform with respect to the superlamellar texture.

4.2 Small angle X-ray scattering (SAXS)

In the previous chapter, it was observed that at sufficiently low temperatures, the filled materials have a tendency to undergo lamellar thickening during melting. This implies that the as-crystallised lamellae are further from equilibrium than NB0=NC0. To complement these findings, SAXS was used to estimate the lamellar long period of the (predominantly branched) material upon quenching. The data were collected using the small-angle beamline 2.1 at the CCLRC Daresbury Synchrotron Source. For these experiments, the beam diameter was ~300 μm, the radiation had a wavelength of 0.154 nm and the sample-detector length was 3.15 m. A Rapid 2-D gas detector was employed. As with the WAXS data in Chapter 2, the images were essentially isotropic, and so they were averaged over an azimuthal range of ±10 ° centred on 0 °. The results are shown in Figures 4.1 and 4.2 below.

The peaks close to 0.06 nm^{-1} indicate a characteristic lamellar long period of ~11 nm, which is a reasonable value for a BPE-rich system [4.1]. Any subtle sample-to-sample variations which may be present cannot be measured as the traces are dominated by increased scatter at low Q-values. However, they are sufficiently small so as to conclude that the lamellar long period is dominated by polymer-polymer interactions rather than polymer-clay interactions.

The increased intensity at low Q-values is informative insofar as it can be attributed to MMT clustering [4.3]. Interestingly, there is little difference between NB10 and NB20, and it is also informative that on this interpretation the NC20 system shows more clustering than the poorly dispersed reference sample! Taken together with the WAXS and TEM data of Chapter 2, we have mounting evidence that the particle size and spatial distributions are very different between the Nanocor- and Nanoblend- based materials. Comparison of the filler distribution and macroscopic lamellar morphologies could provide much insight into the nature of the underlying clay-PE interactions.

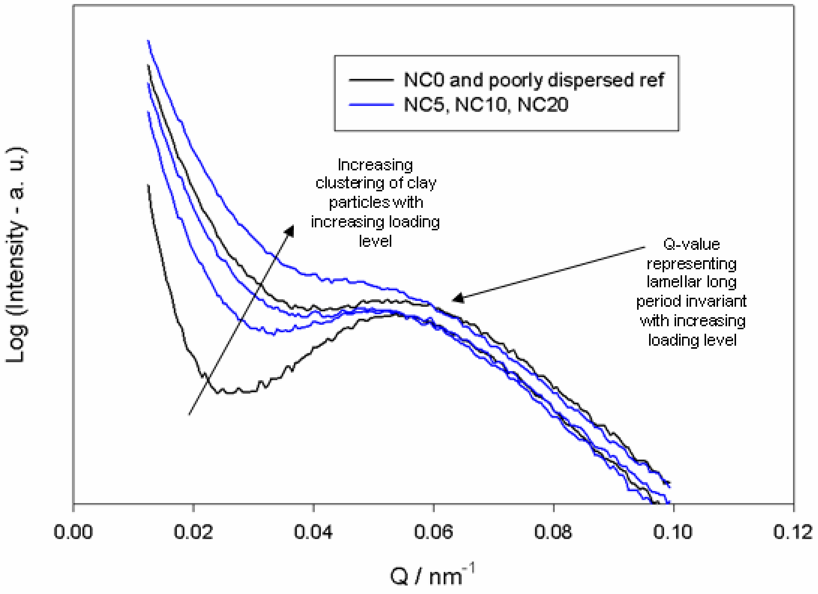

Figure 4.1: SAXS plot for Nanocor-based blends. Arrow indicates direction of increasing clay content. Lower and upper black plots respectively are NC0 and the poorly dispersed reference sample respectively.

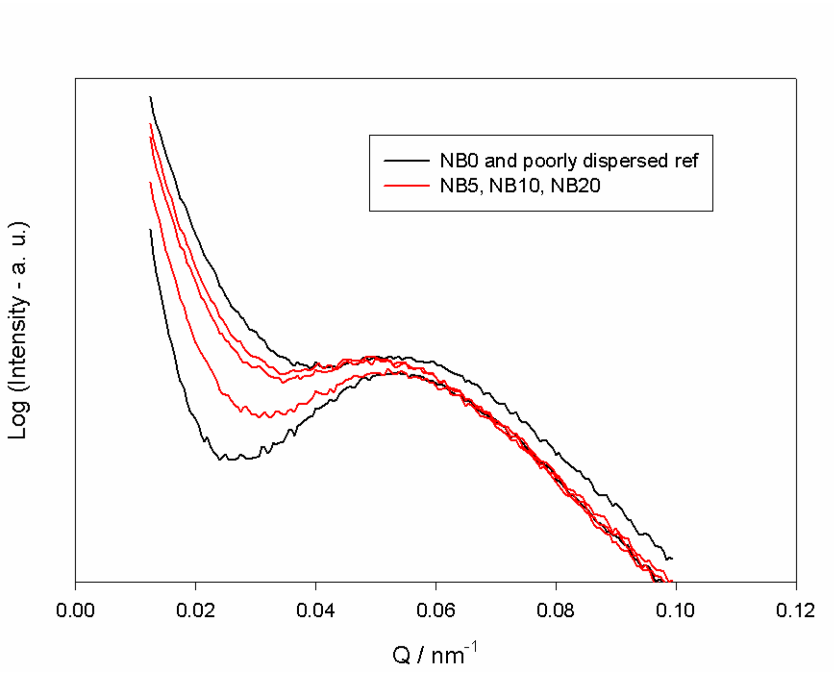

Figure 4.2: As per Figure 4.1 above, but for Nanoblend-based blends. In both cases, the clay induces disorder into the system which varies monotonically with loading level, but the lamellar long period does not appear to change.

4.3 Scanning electron microscopy (SEM)

Fundamentally, there are two ways of obtaining a microscopic image. Photons and electrons both exhibit wavelike behaviour, and so can be refracted by a system of lenses so that each point on the object can be viewed simultaneously. Alternatively, the sample can be scanned such that at any given snapshot in time, only a nominally single point is being measured. Scanning probe microscopy (SPM) begun in 1981 with the invention of the scanning tunnelling microscope; this field now includes a wide range of different techniques from scanning ion-conductance microscopy to atomic force microscopy [4.4]. SEM is a combination of both approaches, although it predates SPM by nearly 50 years [4.5].

In SEM, a beam of electrons is focussed onto the surface of the sample by means of condenser and objective coils. The resolution of this spot is maximised by the use of stigmator coils, which are adjusted manually. The spot is then rastered over the sample by scan coils. The incident electrons penetrate up to 1 μm into the material, undergoing multiple scattering. These primary electrons can only provide spatial resolution down to ~1 μm. It is rather the secondary electrons that are most useful, by virtue of their low energies (~30 eV.) They are able to escape only from the upper 50 nm of the sample (in polymers), resulting in much higher resolution. They are collected with high efficiency by biasing the collector to +400 V. Finally, the production of secondary electrons is highly sensitive to surface topology – i.e. the specific surface area per nominal surface area. Hence, if the surface topography can be made to represent the internal morphology, a good picture can be built up of the internal morphology of the sample.

4.4 Establishment of sample preparation protocol

Since the surface morphology of a polymer should not be assumed to represent the bulk, it was necessary to cut the sample carefully to produce a representative surface. Though some have used the simpler method of fracture surfaces, where the sample is immersed in LN_2 and struck with a hammer and razor blade, Olley *et al.* [4.6] remark that such surfaces are biased. Lamellae are preferentially exposed in the a-direction, whereas the b and c-directions are mostly unrepresented. Microtomy provides a much more reliable means of providing representative morphologies. A similar microtomy procedure was followed as for the TEM work, though the actual operation was much easier and quicker due to the thicker sections that could be cut. Initially, large (5 μm) steps were used, followed by fine (1 μm) steps with the better knife for fine preparation. Twenty of each step length were used to ensure good quality surfaces.

Having generated an appropriate surface morphology, a surface topograph was generated by permanganic etching. A standard procedure was developed at Reading University in the 1980s by Olley *et al.* [4.7-4.9], using acidic solutions containing potassium permanganate. The primary motivation was to provide a technique to complement chorosulphonation for use in transmission electron micrography (TEM). Whereas chlorosulphonation reveals lamellar orientational information at the expense of morphological detail, permanganic etching reveals the morphology at the expense of orientational information [4.9]. It was found that excellent topographies could be produced for SEM, as amorphous material is attacked preferentially to crystalline material. (Olley *et al.* also found that etching takes place preferentially at the fold surfaces of lamellae compared to the ends.)

Two etchants were used in this research:

Etchant 1: 1% w/v $KMnO_4$: (1:2 v/v H_3PO_4 : H_2SO_4)
Etchant 2: 1% w/v $KMnO_4$: (1:2:5 v/v/v H_2O: H_3PO_4: H_2SO_4)

It is believed that that the active species is O_3MnOSO_3H. The phosphoric acid was included to mitigate against the formation of artefacts, tentatively suggested by Olley to consist of $Mn_2(SO_4)_3{\cdot}H_2SO_4{\cdot}4H_2$. Whereas etchant 1 serves the purpose of a chemical “polish,” the addition of water in etchant 2 results in a more aggressive reagent that is better at distinguishing between ordered and disordered regions. In practice, it was found with some samples that clay damage to the knife required the sample to be immersed overnight in etchant 1 to remove the knife marks. The samples were subsequently immersed in vials containing ~10 ml of etchant 2 and placed in a shaker for 2 hours.

The liquid contents of the containers were then poured into a 1 l beaker of cold water to dilute the acid, changing the colour of the dark green mixture from green to purple as the oxidation state of the manganese was altered. The resulting solution was then backwashed onto the sample, preventing surface distortion due to excessive heat generation. Hydrogen peroxide was then added to the beaker (subsequently backwashing the samples) to destroy the permanganate completely prior to disposal down the sink with plenty of running water. The samples were washed three times in distilled water, for cleaning, followed by twice in methanol, for drying. They were then sputter coated with gold.

It is necessary to coat samples for SEM examination with gold. This is because during SEM examination, a path to earth must be provided for the beam electrons. Sputter coating makes use of a gold cathode operating in the glow discharge of an argon atmosphere. Ionised argon atoms are accelerated towards the cathode, eroding gold ions from the surface. The density of the gas must be large enough to produce a sufficient avalanche current, but small enough such that the argon ions have a sufficiently large mean free path to acquire enough momentum. The gas should be sufficiently dense so that the gold ions diffuse through the gas, producing a so-called “cold coating.” Otherwise, their kinetic energy might transfer too much thermal energy to the sample, causing damage [4.10]. Magnetron assemblies are used in modern systems, whereby the gold ions are channelled onto the sample surface by means of a switched magnetic field.

An Emitech K550X coating unit was used with an Edwards E2M2 high-vacuum pump. The chamber was evacuated to 0.1 mbar before being filled with argon to 1 mbar. Coating was carried out at 25 mA for 2.5 minutes. Neglecting cathode heating, deposition rates are proportional to current, implying a film thickness of ~20 nm at 7.5 nm min^{-1}.

A Cambridge Stereoscan 360 was used for this research. The electrons were produced by thermionic emission from a tungsten filament at ~2.7 A. The column was evacuated to ~10^{-6} torr using a turbomolecular pump. This was necessary because electrons are easily scattered in air. A gun voltage of 18 kV was used, with a working distance of 17 mm. At high levels of magnification, there was a high probability of damaging the sample due to electron beam heating. The resulting thermal expansion of the gold would cause cracking, so it was important not to use an area of the sample which would subsequently be subject to examination. Having set the brightness and contrast at appropriate levels, the signal was sent to a PC for recording. Half the normal scan rate (TV/32 as opposed to TV/16) was used for improved picture quality.

The crystalline morphology of NB0=NC0, seen in Figure 4.3, is typical for this blend composition, with a small nucleation enhancement resulting from a relatively mild shear history [4.11-4.12.] A section through a spherulite is outlined in red as a reminder that spherulites are 3-dimensional objects: non-diametral sections of impinged objects will not necessarily be circular. At higher nucleation temperatures around 120 °C, the nucleation density is smaller and the overall texture less space-filling. At even higher temperatures, sheaf-like objects are seen which, in terms of the underlying growth processes, are simply immature spherulites [4.13].

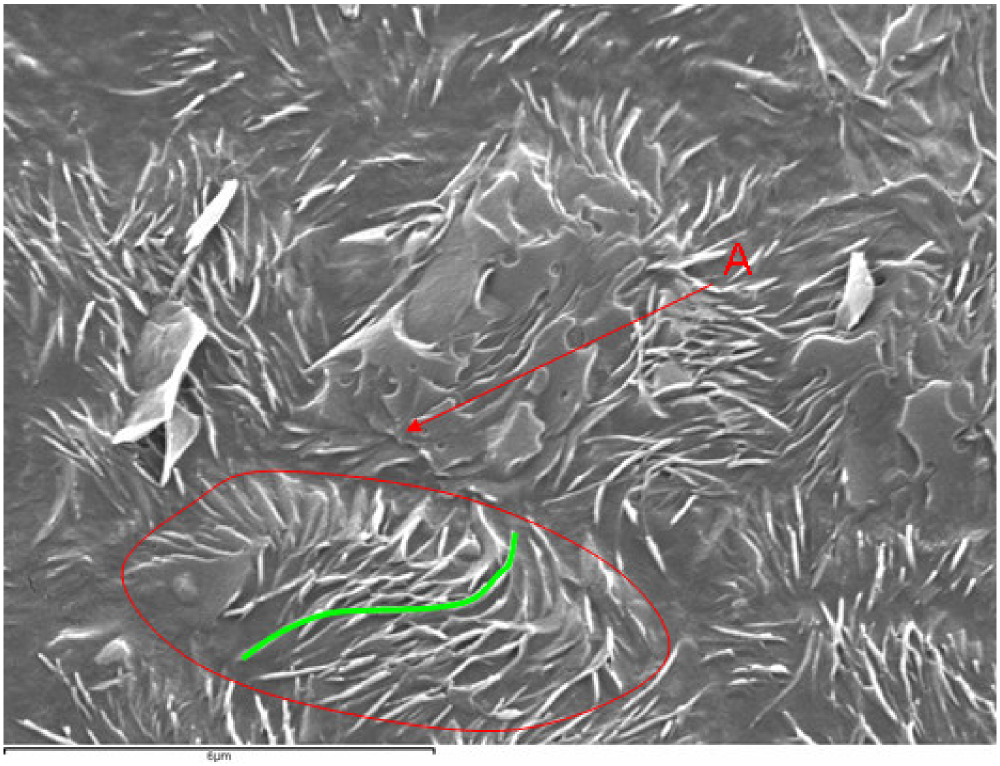

Figure 4.3: NB0=NC0, crystallised at 117 °C. A screw dislocation is seen at the bottom left of the centre spherulite (A). Another spherulite boundary outlined in red. Green curve follows a dominant lamella.

Figure 4.4 represents the morphology of the poorly dispersed reference sample. An incompatibility is evident between poorly dispersed clay particles and the polyethylene matrix. Furthermore, the shape and size distribution of the spherulites, which at 119 °C are nearly space-filling, are unaffected by the presence of the clay. On the left hand side, the polyethylene has pulled away from the surface of the clay (arrow A); this could be a consequence of solvent evaporation, thermal contraction or preferential etching due to capillary action. A slight flow-field history is still observed in the matrix around the upper tip (arrow B), where a measure of lamellar orientation can be seen.

In order to optimise the etching process for optimum clarity of both matrix and filler, the level of $KMnO_4$ was varied. It was considered too dangerous to increase the level due to the risk of explosion, and so concentrations of 0.3 %, 0.1 % and 0.03 % and 0.01 % were tried. As expected, the 0.3 % and 0.1 % level simply resulted in blurred images. The lowest concentrations were particularly unsuccessful as the mixtures were

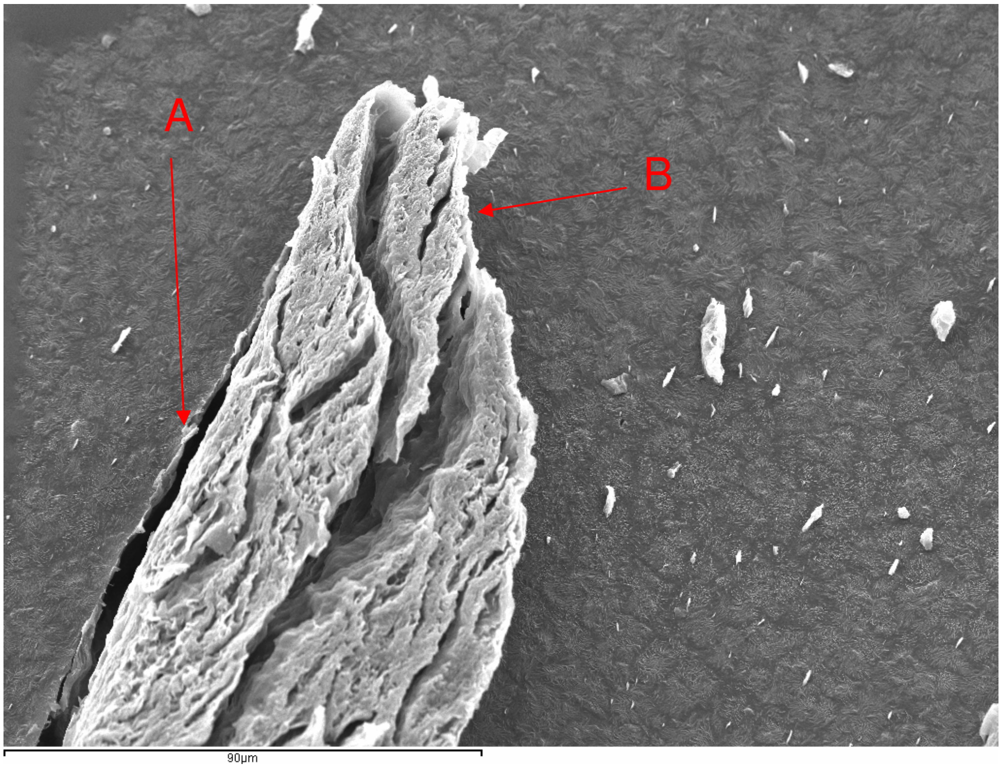

Figure 4.4: Poorly dispersed reference sample, crystallised at 119 °C. The large clay particle is seen to be incompatible with the matrix (A). Flow effects are seen in the matrix around the upper tip of the particle (B).

highly sensitive to deactivation by residual water, typically within several minutes.

Generally, it was only possible to obtain informative images of the isothermal, rather than the quenched, lamellae. On the other hand, Figures 4.5 and 4.6 show the effect of exposing MA-NB10 and MA-NB0 to an etch containing 0.1 %wt $KMnO_4$. These images provide further evidence for the particle size distribution of the Nanoblend-based samples. Figure 4.5 consists of large flaring objects oriented to the extrusion field with an apparent width of ~ 200 nm. Flaring is a result of high local surface gradients (ie edge-on lamellae or platelets) giving rise to high electron yields and saturator detection. The real width of these objects is likely to be the same as the surrounding non-flaring objects, namely 20-50 nm. On the reasonable assumption that this disordered morphology, which is absent from Figure 4.6, consists of clay tactoids and / or polyethylene lamellae, we can conclude that a large fraction of the clay particle size distribution in the Nanoblend-based

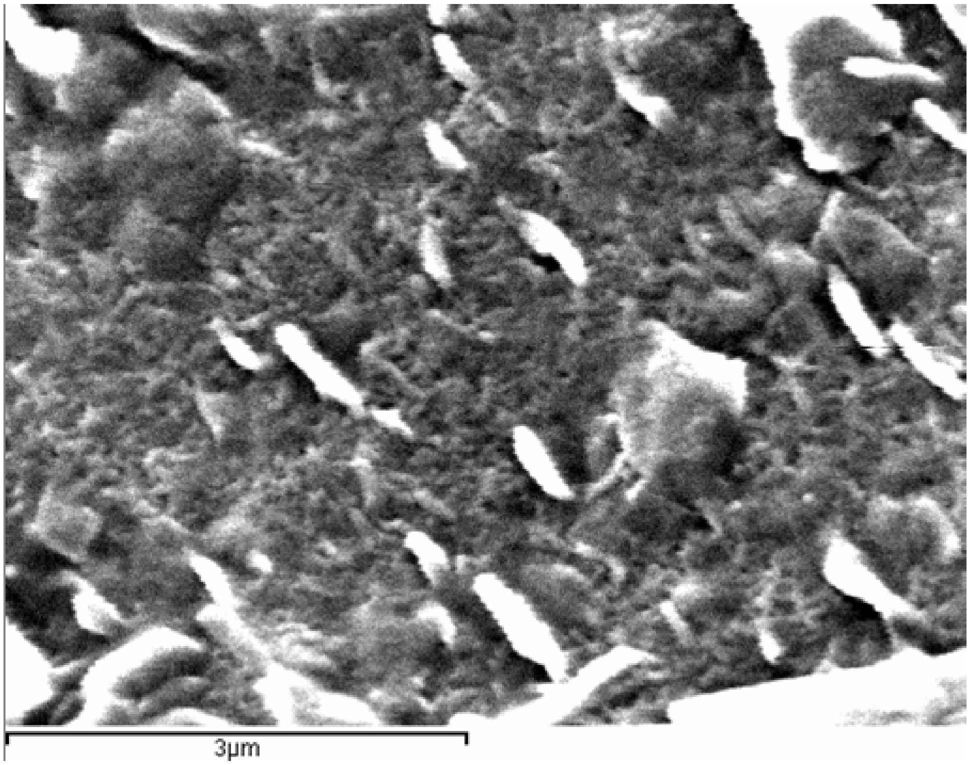

Figure 4.5: Space between sheaves of NB10 (MA), crystallised at 119 °C. Flaring clay particles are embedded in a highly disordered matrix.

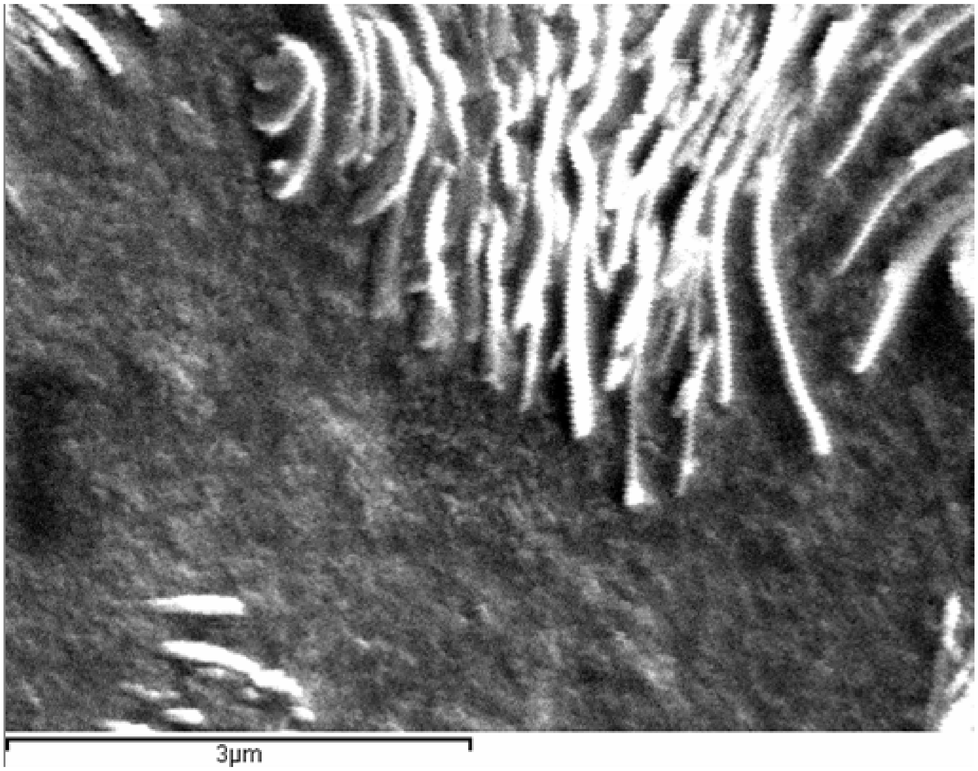

Figure 4.6: As Figure 4.5, but for MA-NB0. The flaring lamellae belong to a sheaf-like object.

samples is of a similar size to the polyethylene lamellae. Unfortunately, it was not possible to reproduce this effect in any of the non-maleated blends. However, this result does suggest that suitable development of etchant chemistry could provide a means of analysing a broad range of hierarchical clay distributions in polymer nanocomposites.

4.5 Initial investigations on the unfilled and 10 parts-filled materials

Figures 4.7-4.9 demonstrate the differences in the clay particle size distribution at the upper end. One could be excused for mistaking NB10 to be an unfilled sample containing merely accidental inclusions. Conversely, some of the clay particles in Figure 4.9 are of the same order of magnitude as the largest seen in the solution blended sample! This is consistent with the high level of low angle scattering in the Nanocor-based materials as judged by SAXS, reinforcing the assertion that X-ray scattering in this Q range is indeed

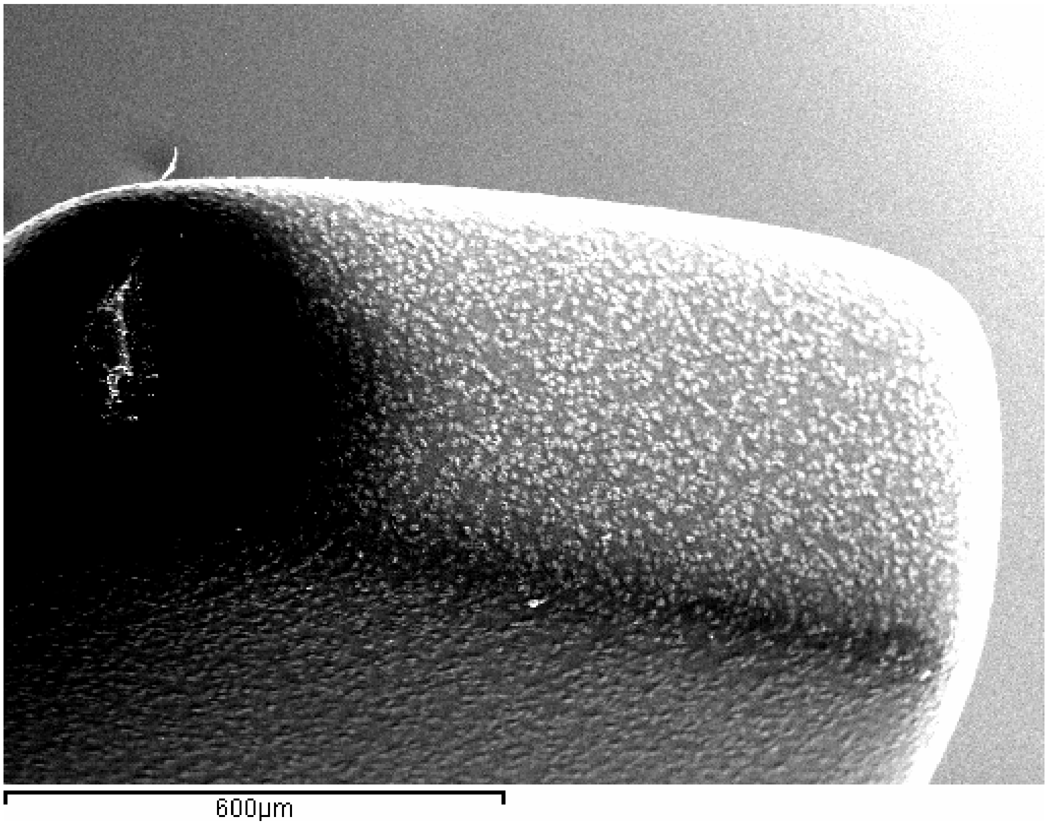

Figure 4.7: NB0=NC0, crystallised at 124 °C. An even distribution of sheaves is observed.

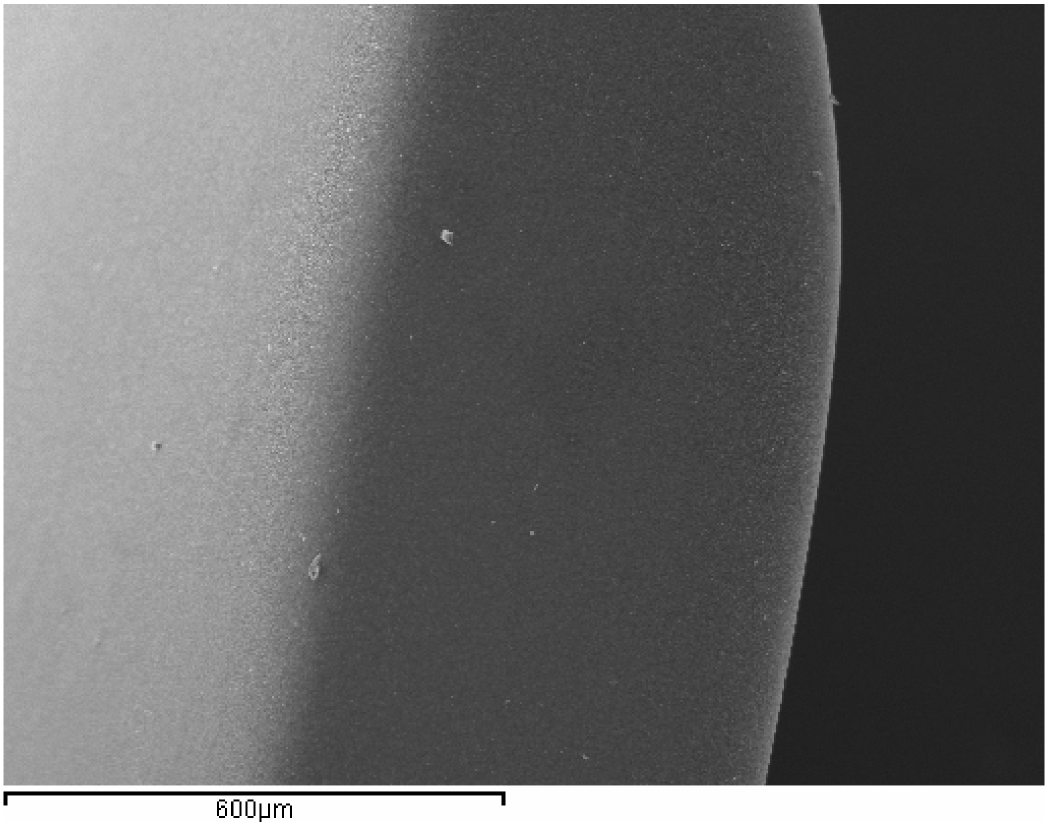

Figure 4.8: NB10, crystallised at 120 °C.

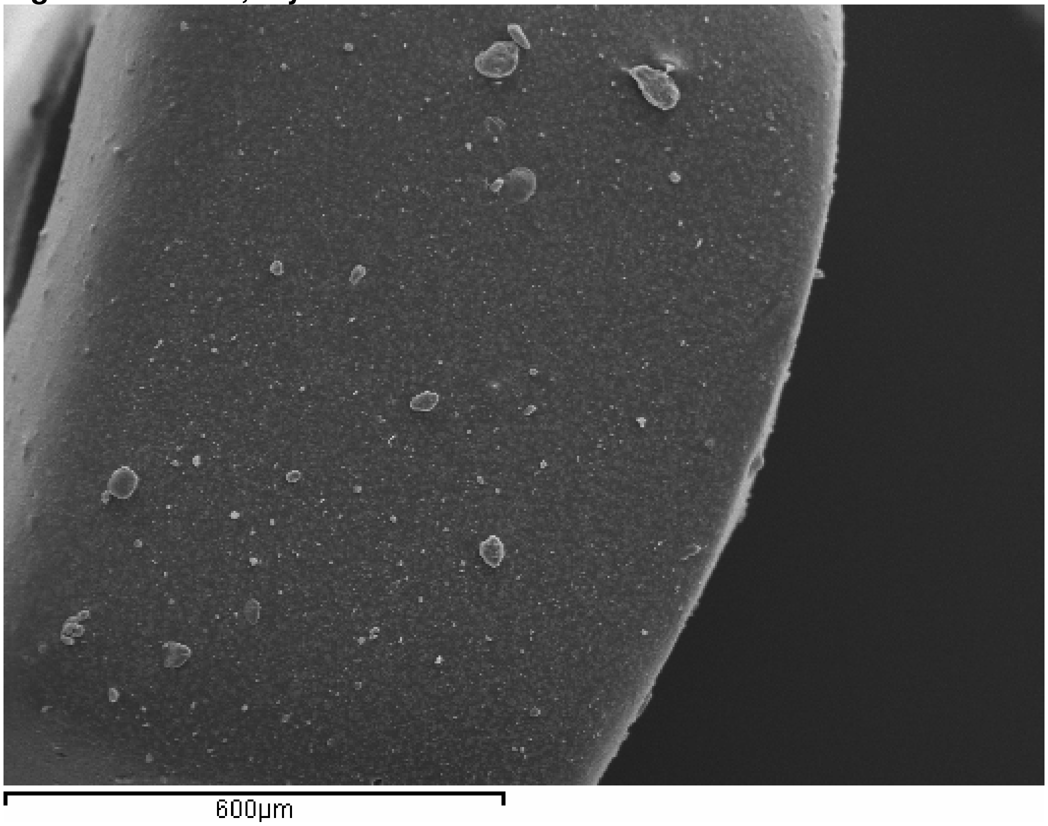

Figure 4.9: NC10, crystallised at 120 °C. Large clay agglomerations are seen in this material, in contrast to NB10 above.

associated with the aggregation state of the MMT.

Figures 4.10-4.18 show the superlamellar morphologies of the unfilled and 10 parts-filled materials as a function of isothermal crystallisation temperature. Beginning with a crystallisation temperature of 124 ℃, NB0=NC0 exhibits a morphology in transition between sheaves and spherulites. Comparing Figure 4.10 with the idealised sheaf of Figure 4.11, “A” and “B” are views down axis 1, “C” being a view down axis 2. Axis 3 would be characterised by S- or C-shaped dominant lamellae present in the circled spherulitic section of Figure 4.3. Quench halos are attached to these objects (arrowed “D”); these correspond to defective linear material which crystallises adventitiously onto the isothermal lamellae during quenching. Conversely, NB10 exhibits behaviour consistent with the PE chain immobilisation hypothesis. Looking down axis 1, the curvature of the lamellae is considerably reduced. Down axis 2, irregular planar growth of the lamellae has given rise to a high density of defects. In contrast, NC10 seems to display behaviour somewhere between that of NB0=NC0 and NB10.

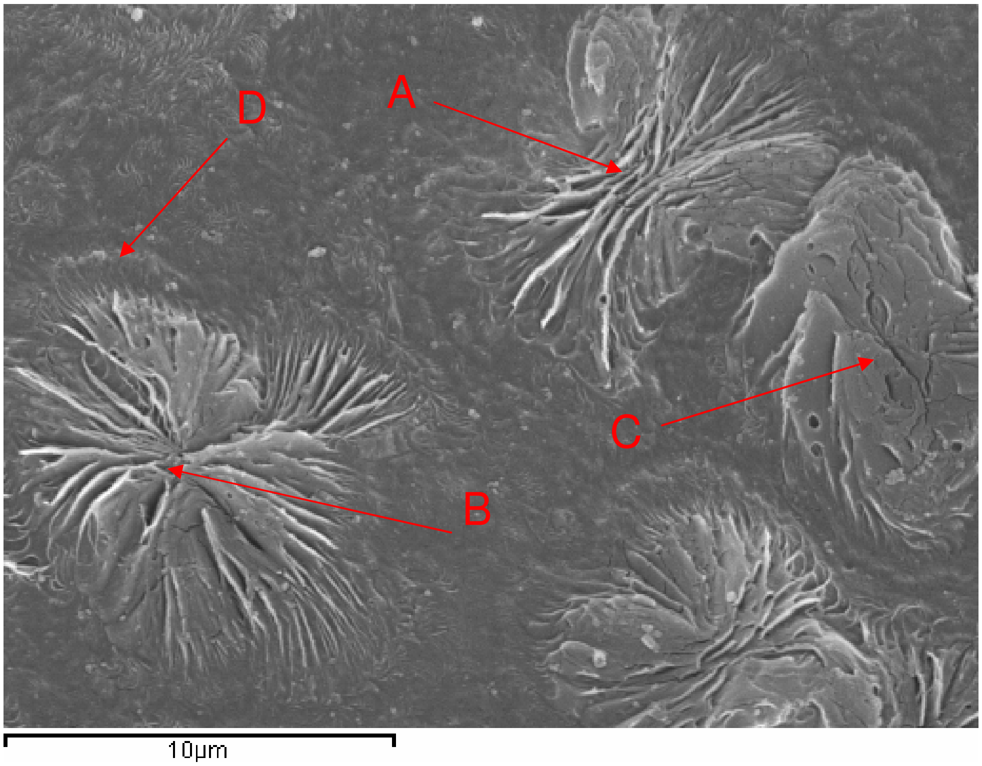

Figure 4.10: NB0=NC0, crystallised at 124 ℃. Classical sheaf morphology together with quench halos.

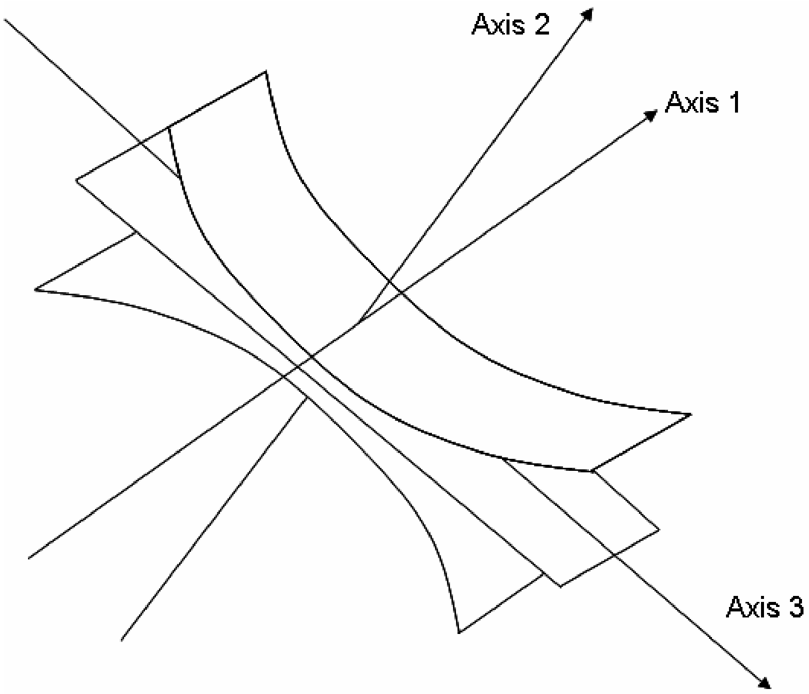

Figure 4.11: Schematic of idealised sheaf to aid discussion in text.

At 117 °C, the effect lamellar growth disturbance in NB10 is seen to largely suppress the banding mechanism otherwise seen in NB0=NC0. NC10, however, is seen to produce a highly nucleated, highly disordered system, in line with the findings of thermal analysis. 120 °C then corresponds to a transition region where nucleation enhancement is not yet associated with massive disorder; here, superlamellar clusters originating from individual nucleation events can still be discerned.

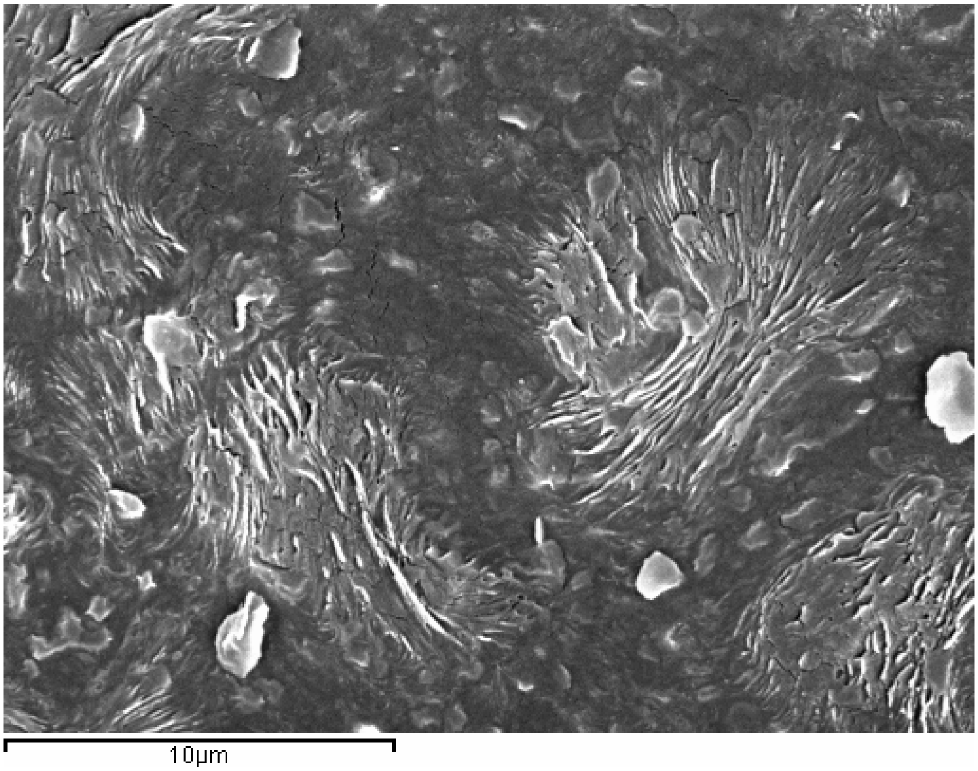

Figure 4.12: NB10, crystallised at 124 °C. Although overall dimensions remain unchanged, sheaf growth is clearly disrupted. Micron-sized tactoids also present.

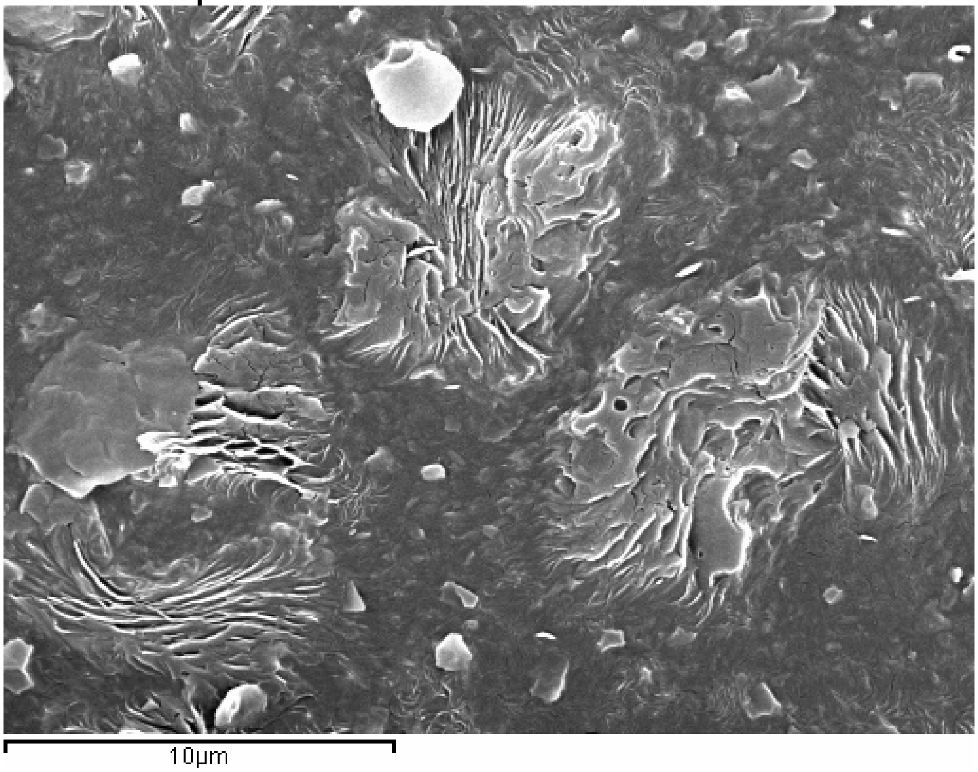

Figure 4.13: NC10, crystallised at 124 °C. Lamellar order does not seem to be as severely disrupted by Nanocor.

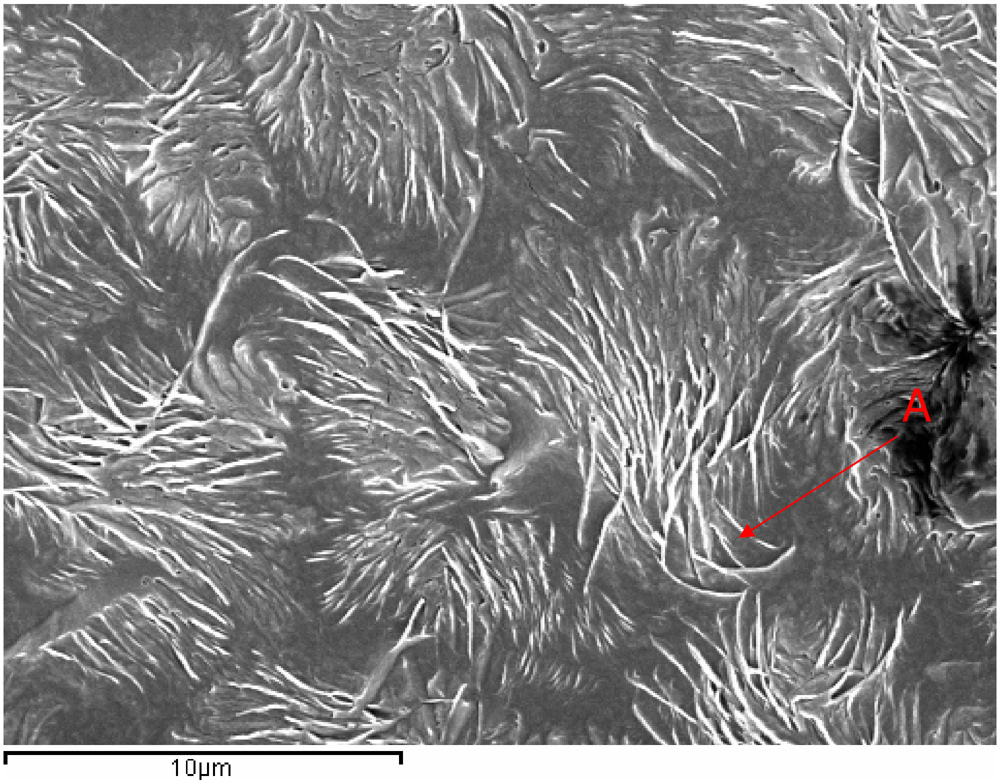

Figure 4.14: NB0=NC0, crystallised at 120 °C. The beginnings of banding can be seen (arrowed.)

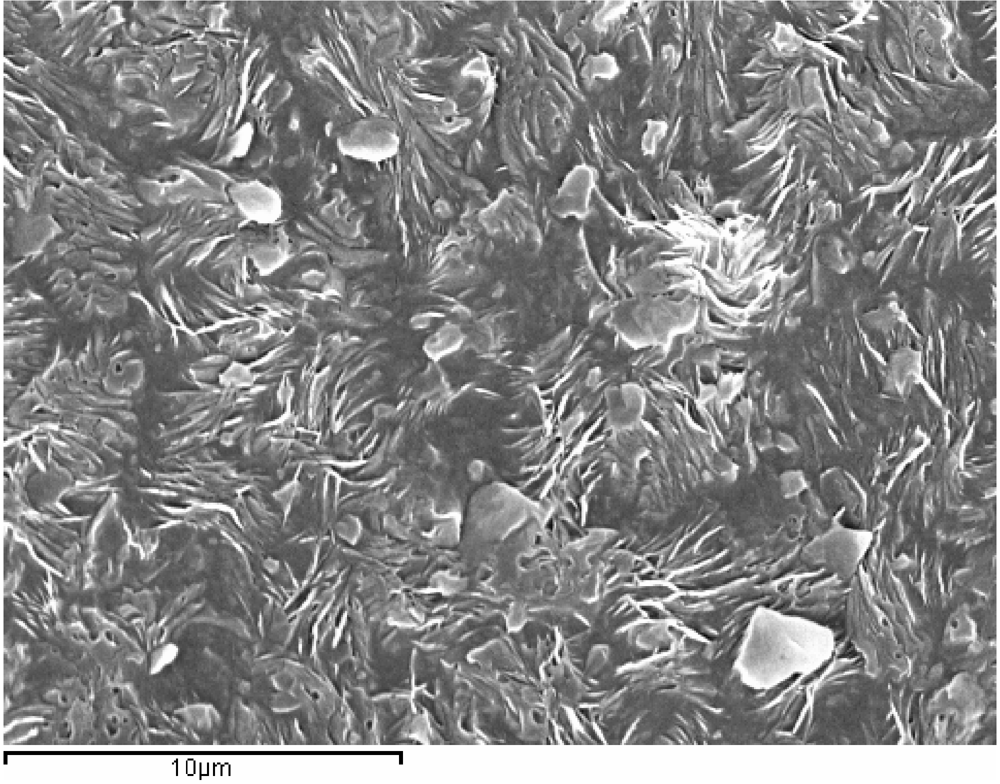

Figure 4.15: NC10, crystallised at 120 °C. An increase in structural disorder AND an increase in nucleation density can be seen.

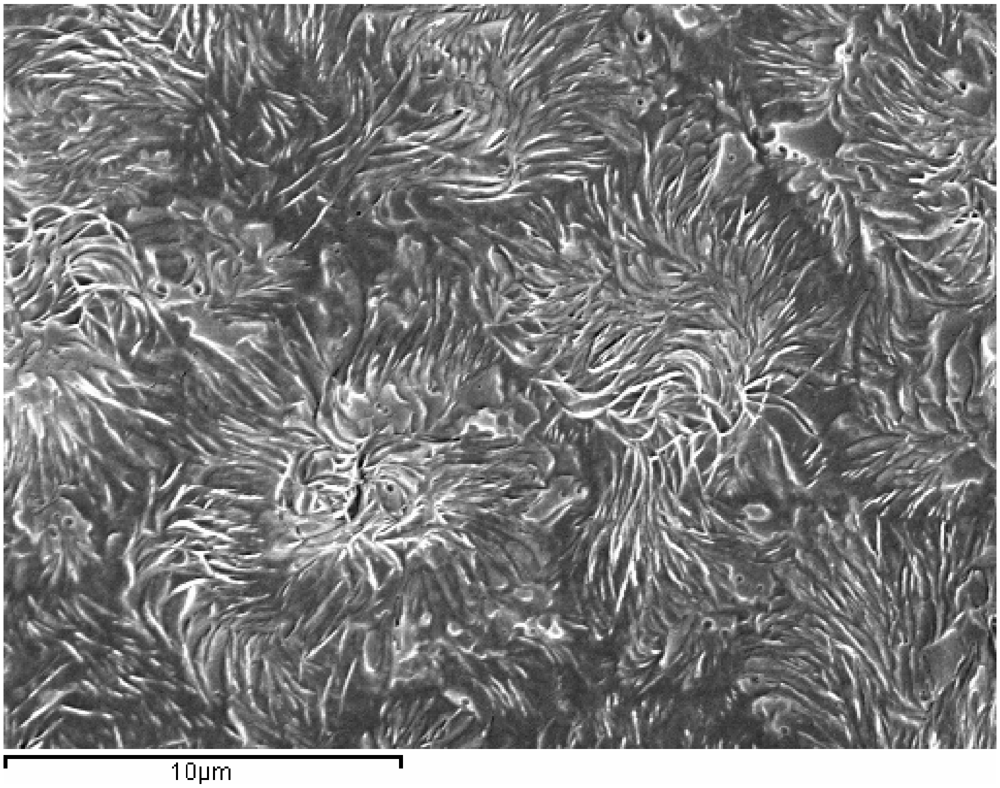

Figure 4.16: Banded spherulites are observed in NB0=NC0, crystallised at 117 °C.

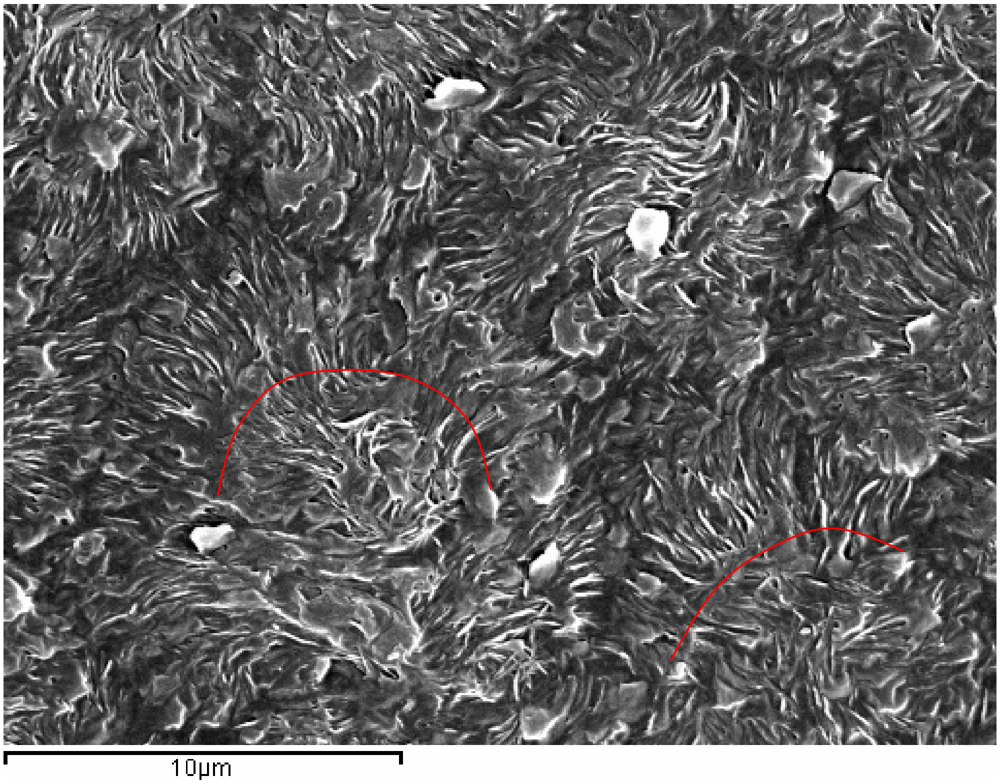

Figure 4.17: NB10, crystallised at 117 °C. Although faint banding can be seen (as indicated by the red arcs), it is much less pronounced than in the unfilled sample.

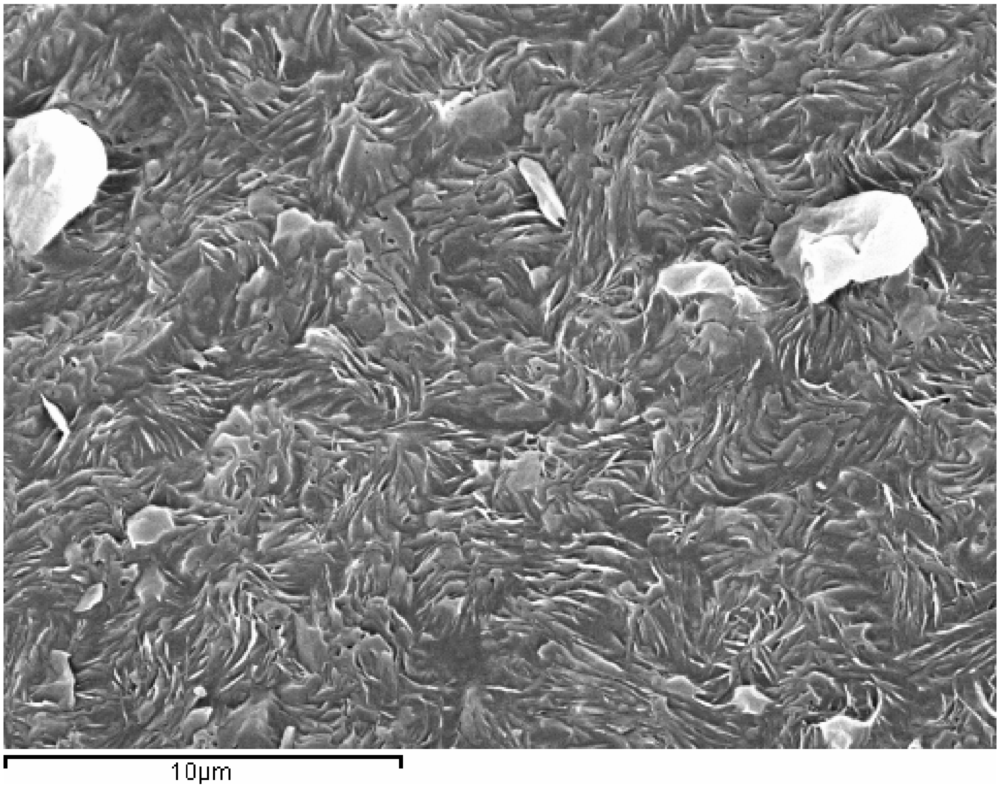

Figure 4.18: NC10, crystallised at 117 °C. A completely disordered, highly nucleated system.

4.6 Influence of loading level on morphology

So far, it has been demonstrated that Nanocor and Nanoblend-filled materials give rise to quite different morphologies. The Nanoblend formulation does not significantly affect nucleation densities, but it does perturb the growth process at the lamellar level. At high temperatures, the Nanocor system produces less morphological disruption, but below 124°C, the nucleation density is massively increased and the growth process perturbed. It was not possible to confirm from DSC that the crystallisation kinetics of NC10 are not enhanced at 124 °C due to baseline drift. The effect of loading level was studied with a view to clarifying these processes. The results are seen in Figures 4.19-4.30.

In the case of NC5, the effect of using a lower loading level is simply to move the onset of enhanced nucleation to lower temperatures. At 120 °C, the only appreciable difference between Figure 4.21 and the unfilled sample is that the beginnings of banding cannot be observed. Even at 117 °C the increased nucleation density is not attended with massive structural disorder.

On the other hand, NC20 displays a highly-orientated non-spherulitic structure at this temperature. A subtle hint of this process can in fact be seen at 124°C by looking closely at the outer regions of the sheaves on the left hand side of Figure 4.20 (arrow B). It is clear that the shear fields experienced during extrusion were sufficient for clay tactoid orientation but not for alignment of the PE chains. This image therefore captures the onset of competition between intrinsic PE growth, dominant at high temperatures, and growth which is biased in the direction of clay sheets, active at lower temperatures.

Whereas low loading levels and high temperatures are able to disable the Nancor crystallisation modification mechanism, this does not seem to be the case with the Nanoblend systems. In the case of NB5, the lamellar roughening effect is still evident at all temperatures (Figures 4.24, 4.26 and 4.28.) Furthermore, close examination of Figures 4.24-4.27 indicates the presence of some very subtle interaction processes. Figure 4.27b illustrates the exception to the above conclusion concerning the general uselessness of using low $KMnO_4$ concentrations. It resolves clusters of secondary lamellae which would be etched away by larger $KMnO_4$ concentrations (Figure 4.27a), but at the expense of blurred clay tactoids and an incapability of discerning the primary lamellae. Essentially, to lower the level of $KMnO_4$ is to reduce the contrast so as to increase the resolution of secondary features. It is therefore of use in specific cases such as this, where the process is too subtle to interpret from the high-contrast primary lamella image alone. This result provides evidence that NB20 fundamentally changes the means by which circular symmetry is achieved in a mature superlamellar object. In NB0=NC0, the required compliance is generated by means of cooperative isochiral screw dislocations leading to the long-range ordering phenomenon of banding. Here, however, the lamellae are constrained in parallel clusters and separated by linear boundaries; these boundaries are sources of compliance for circular symmetry. Whether or not they are a direct consequence of MMT particles constraining the lamellar growth or simply the impingement of neighbouring clusters remains to be seen.

Figure 4.29 is the example *par excellence* of the difference in orientation of the clay and the supercrystalline structures. The sheaf is perpendicular to the flow field and the effect of the clay on its internal morphology is negligible. Figure 4.30 contrasts two high magnification images of one of these sheaves. In the upper image, a small degree of local perturbation has taken place, but the overall trajectories of lamellar growth are unaffected. The lower image provides tentative evidence of clay particles actually being aligned with the growth trajectories, perhaps as a consequence of excluded volume.

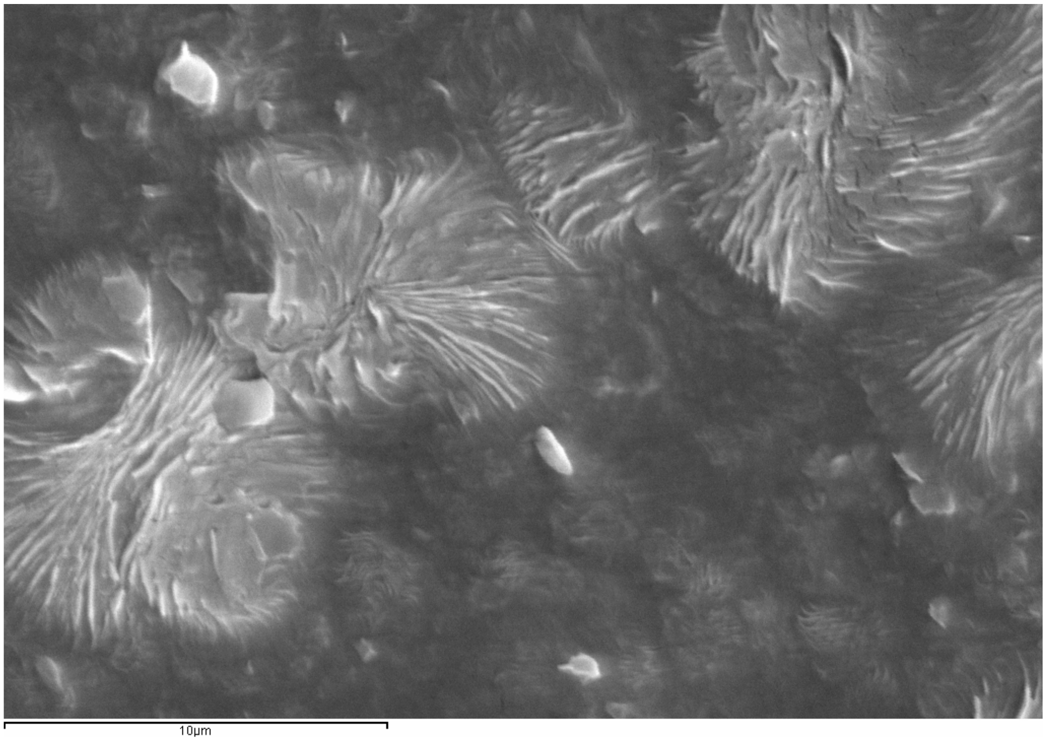

Figure 4.19: NC5, crystallised at 124 °C. Morphology is much closer to the unfilled sample than to NC10.

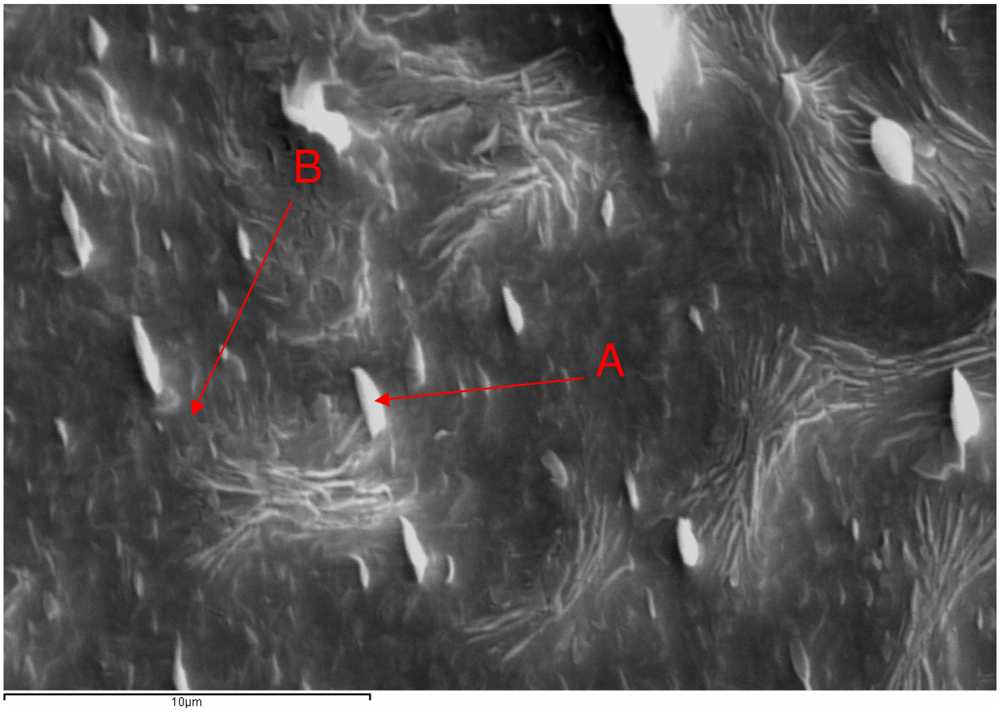

Figure 4.20: NC20, crystallised at 124 °C. Elongated agglomerations of clay (A), together with subtle lamellar orientation effects (B).

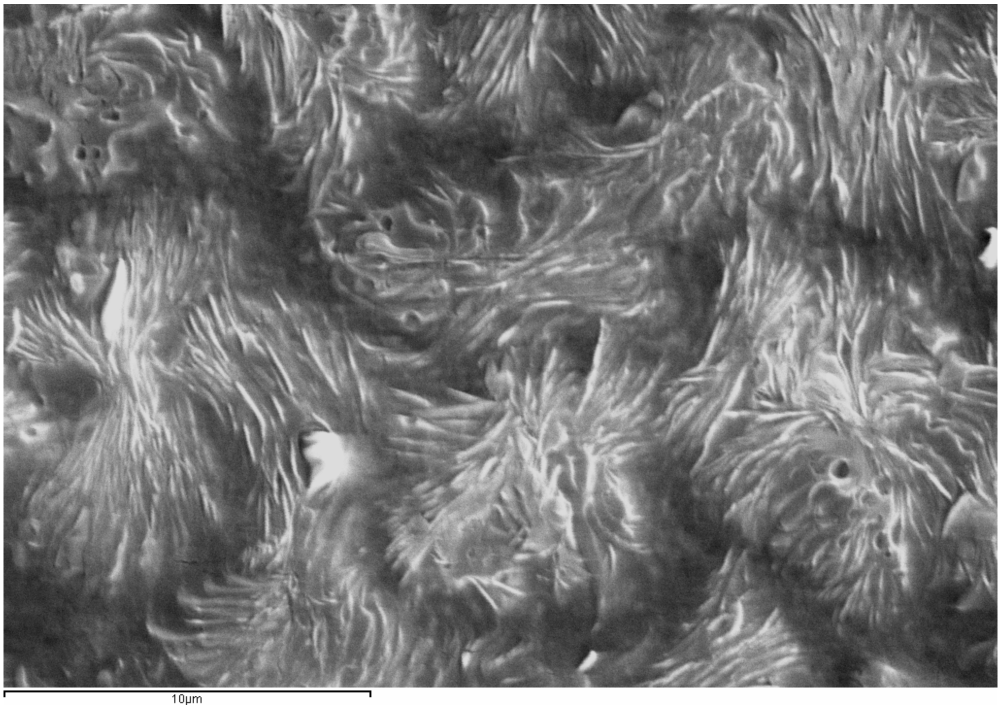

Figure 4.21: NC5, crystallised at 120 °C. Remarkably similar to the unfilled sample, but without the beginnings of banding.

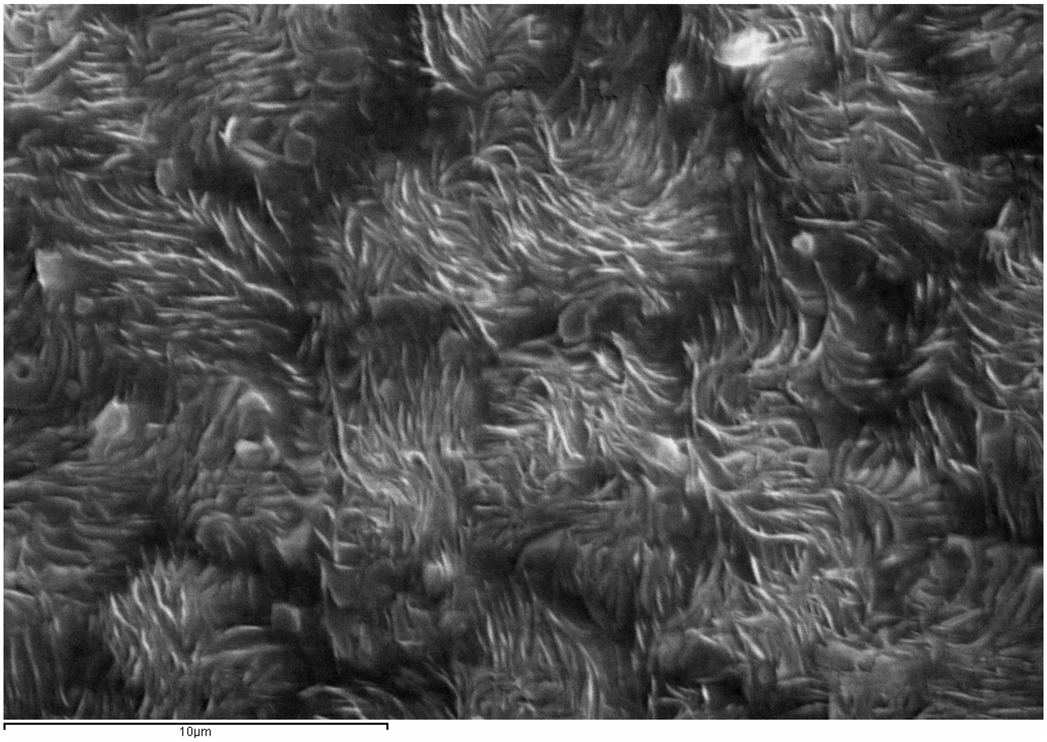

Figure 4.22: NC5, crystallised at 117 °C. Nucleation density is larger than NC0, and the superlamellar agglomerations are smaller.

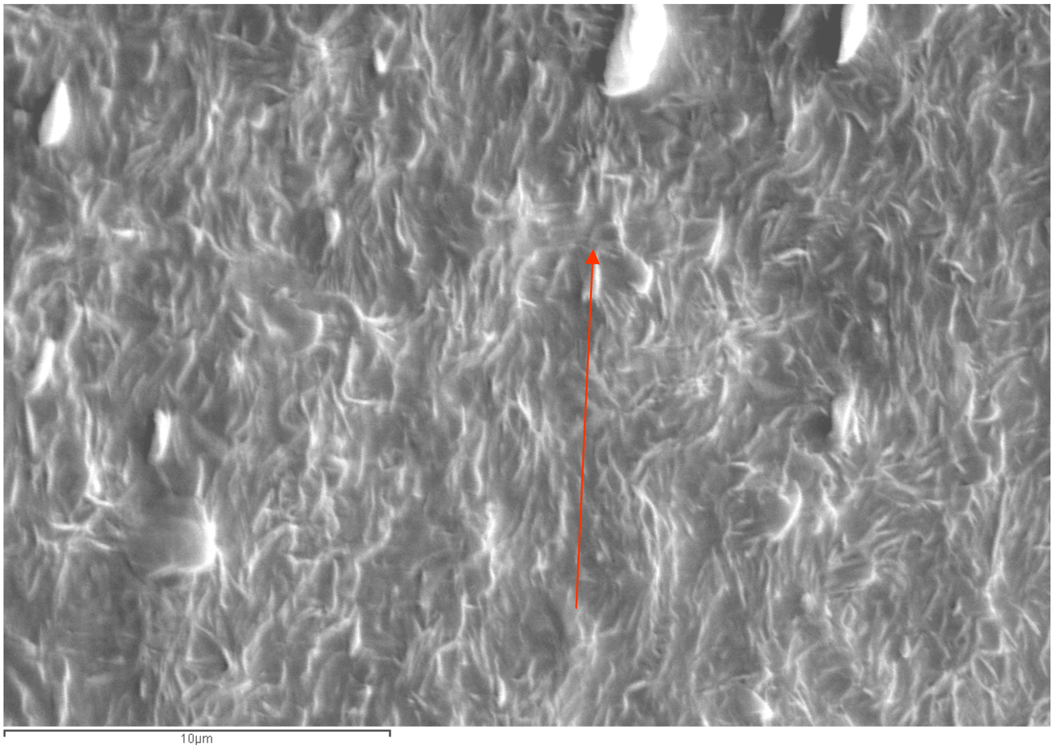

Figure 4.23: NC20, crystallised at 117 °C. A transition has occurred to a highly oriented morphology. Orientation direction arrowed.

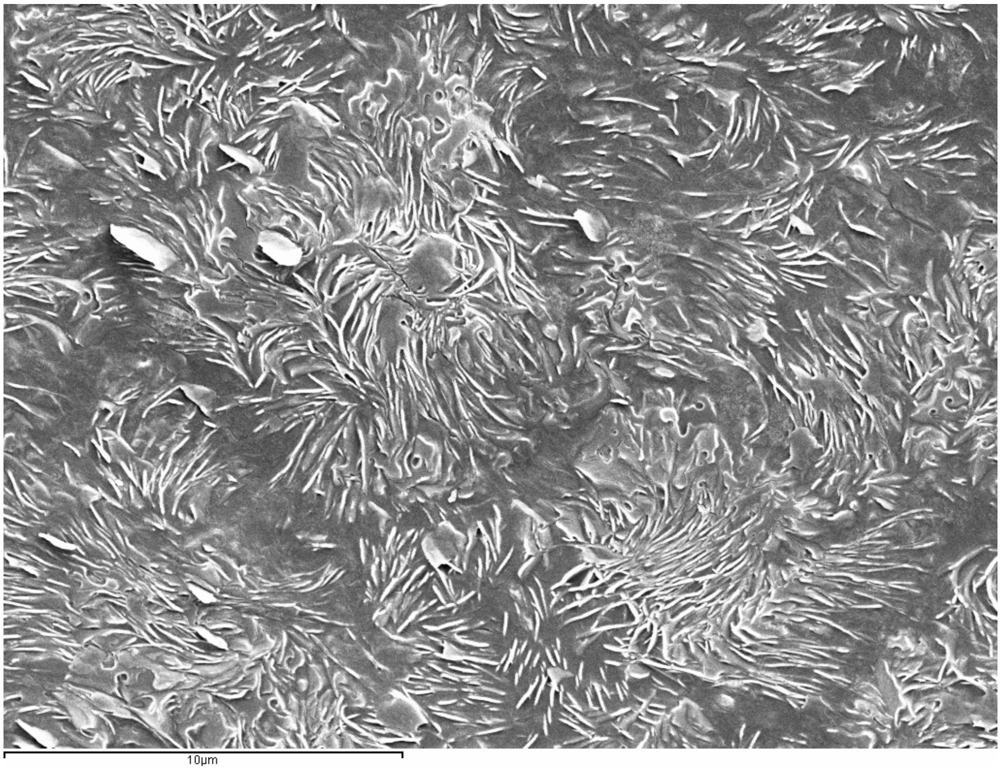

Figure 4.24: NB5, crystallised at 117 °C. Significant disruption is seen even at this low loading level.

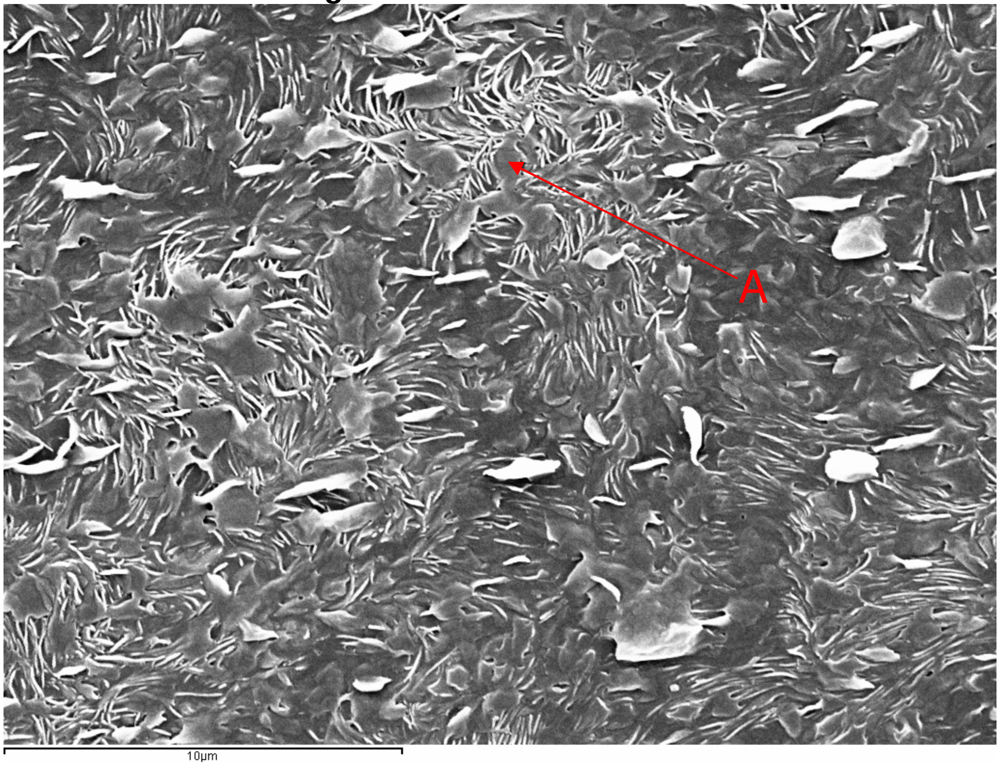

Figure 4.25: NB20, crystallised at 117 °C. Extended sheets of clay are incorporated into the spherulitic structure.

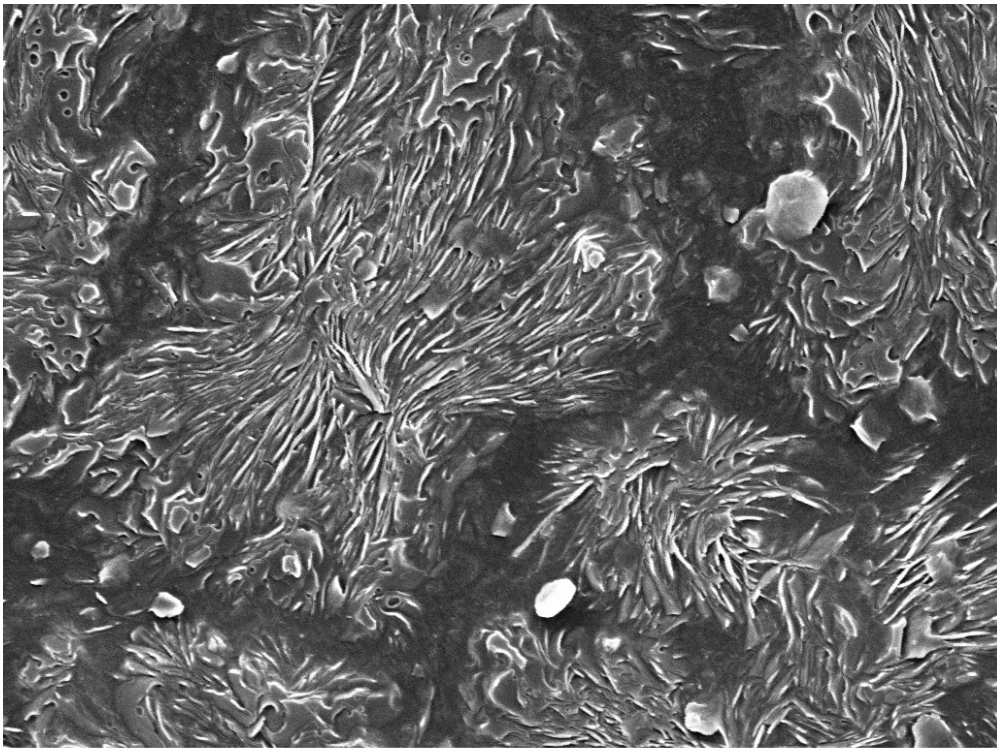

Figure 4.26: NB5, crystallised at 120 °C.

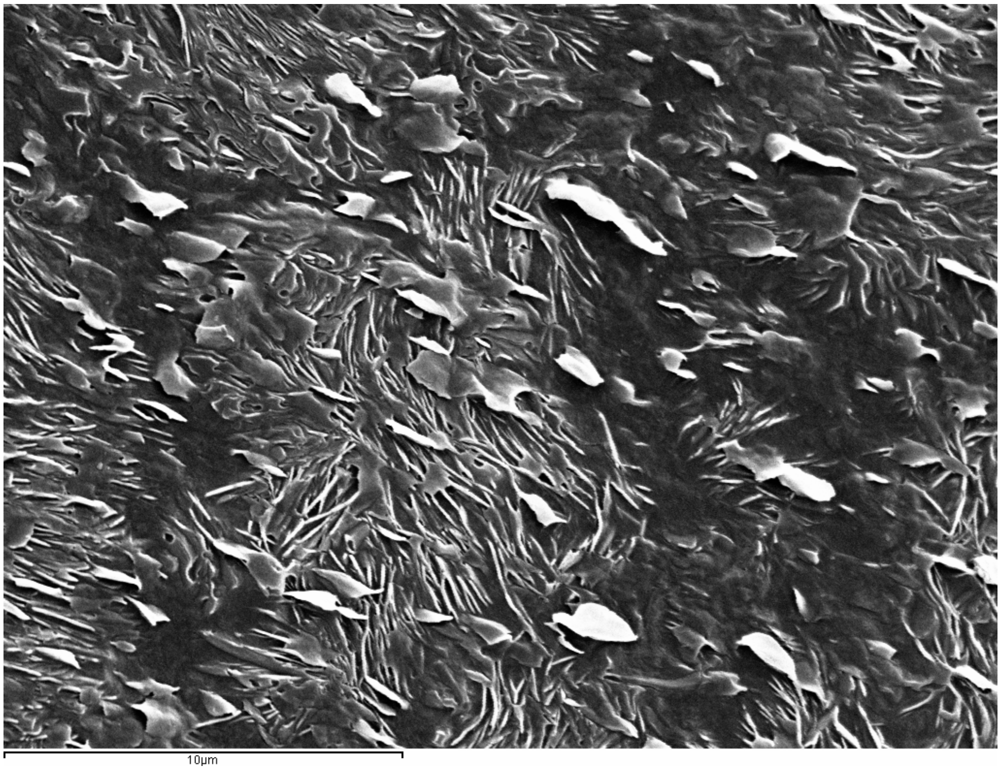

Figure 4.27a: NB20, crystallised at 120 °C. Macroscopic distortion of the supercrystalline objects appears to have taken place.

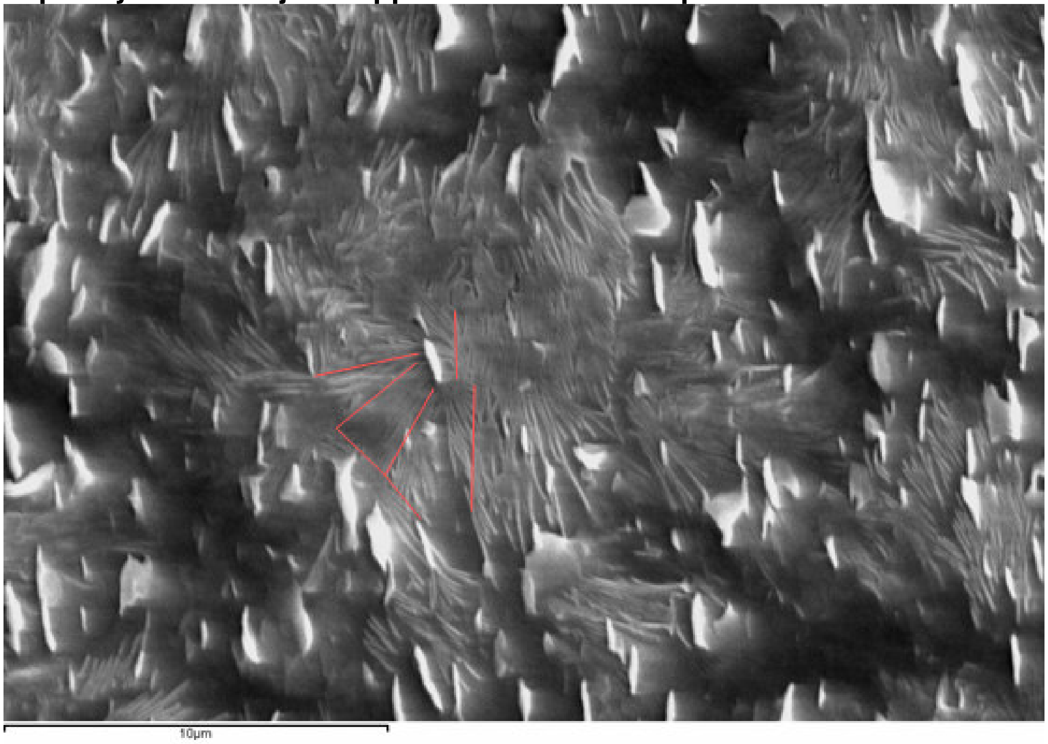

Figure 4.27b: As Figure 4.27a above, but etched with one tenth the concentration of $KMnO_4$. Distinct boundaries are seen between groups of parallel lamellae; a selection of these illustrated in red.

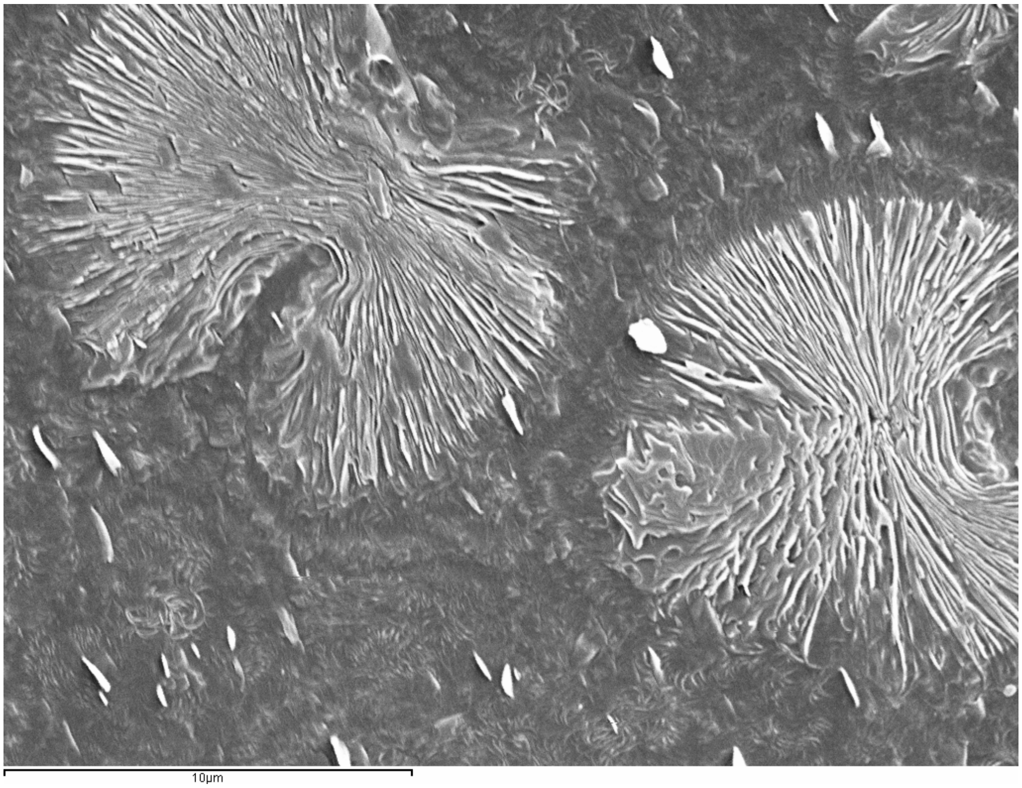

Figure 4.28: NB5, crystallised at 124 ℃. The sheaves are slightly larger, and are composed of straighter lamellae, than NB0=NC0.

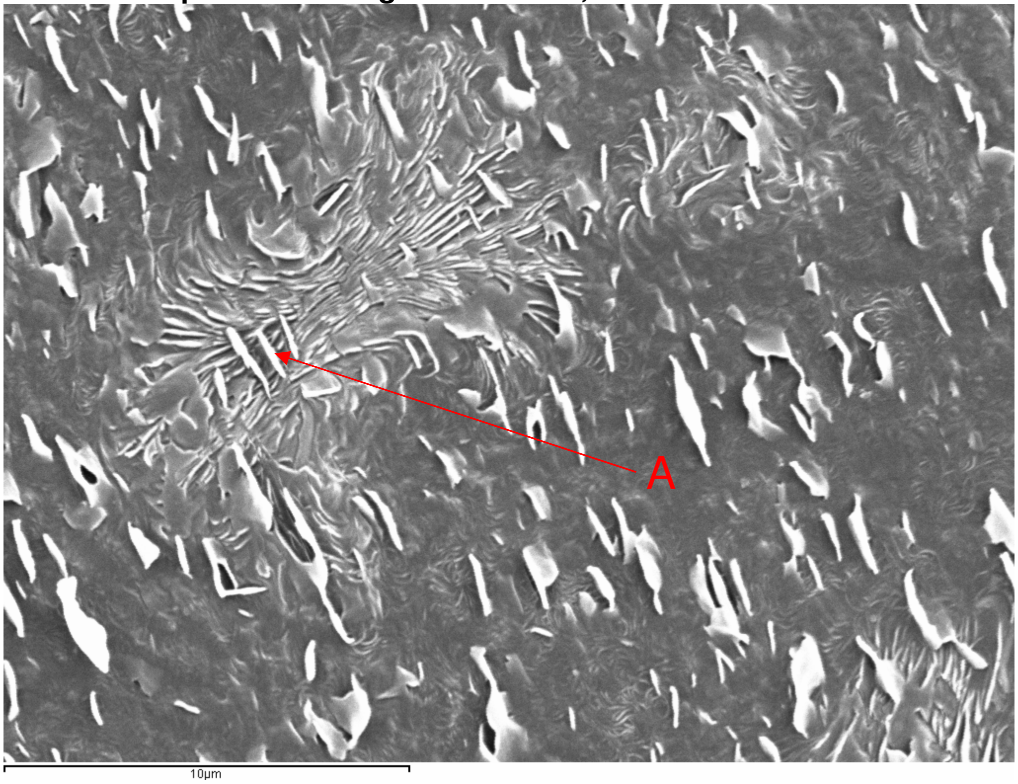

Figure 4.29: NB20, crystallised at 124 ℃. A striking example of tactoids orientated in the flow field, yet at most only disturbing the local order of the sheaf (A).

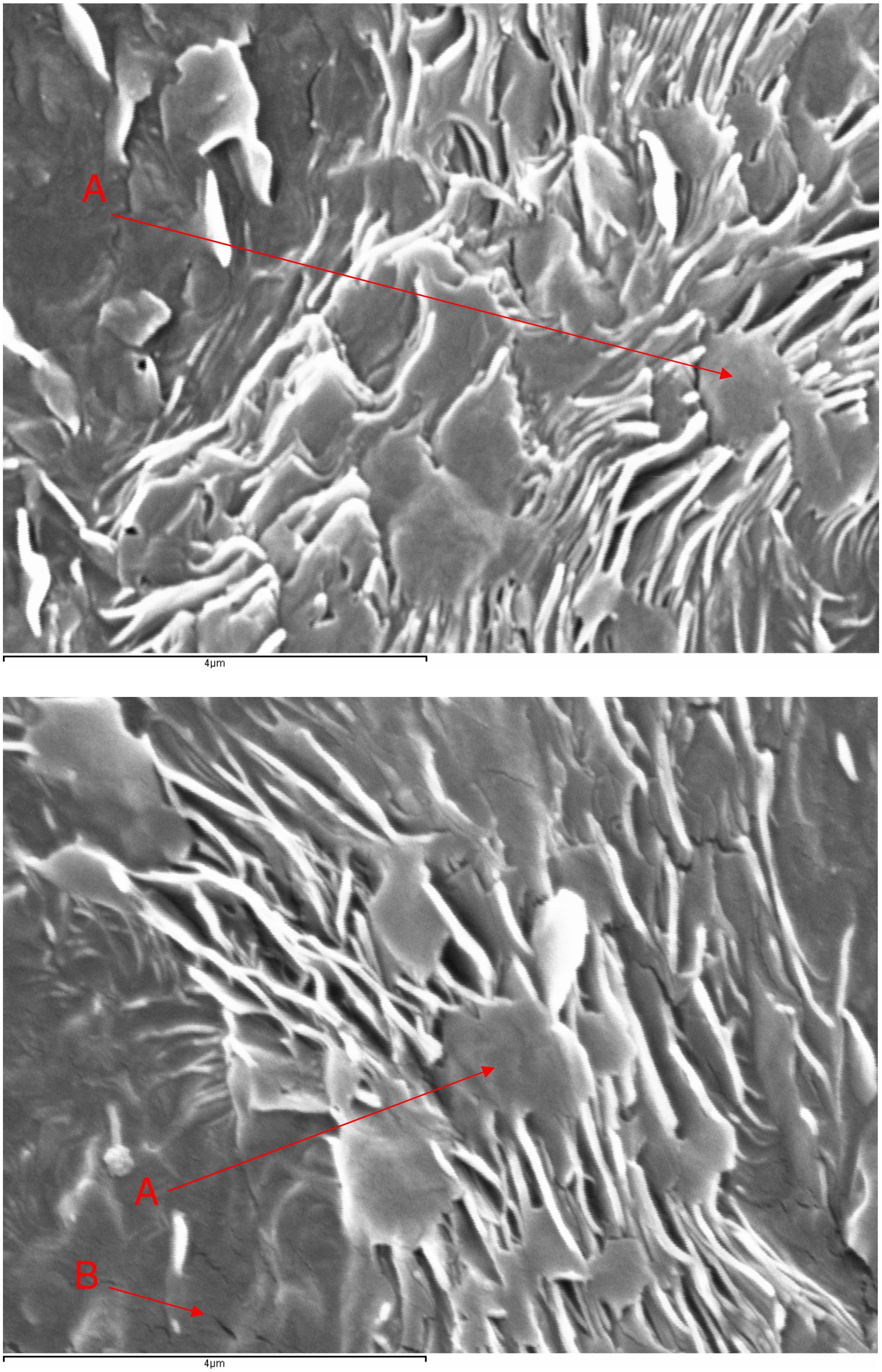

Figure 4.30: Very high magnification images of NB20 crystallised at 124 °C. Incorporation of clay platelets into the lamellar growth process is seen.

4.7 Discussion

The conclusions of the previous chapter pertaining to the isothermal crystallisation kinetics are complemented here. Specifically, the Nanocor-based systems are demonstrated to be subjected to massively enhanced nucleation, whereas the Nanoblend-based systems are not. That the level of disorder increases dramatically when the enhanced nucleation mechanism is active argues for a kinetic origin for the disorder via entanglements. On this interpretation, the lack of increase in nucleation density observed in the previous chapter between NC10 and NC20 corresponds to saturation in the level of disorder attainable. It was inferred in Chapter 3 that the Nanoblend also tends to reduce the mobility of the crystallising chains. Kinetically-induced disorder is not seen here, however; it is believed that a more subtle alteration of chain diffusion processes occurs at the thermodynamic level. If this mobility reduction can prevent the reorganisation of fold chains during growth, it would sufficiently explain the lamellar straightening phenomenon observed here, together with the increased density of screw dislocations observed down axis 2.

It may be that the nucleation enhancing mechanism provided by the Nanocor is entirely entropic. Indeed, Nowacki *et al.* [4.14] attribute nucleation in polypropylene-MMT systems to shear fields, commenting that in and of itself, MMT is only weakly nucleating. Shear fields serve to lower entropic barriers to crystallisation through the aligning of polymer chains. The ability of the MMT to nucleate is then related both to its shear history and its particle size distribution: the nucleating activity is both a consequence and cause of disorder. It is believed that individual montmorillonite sheets may interact both through edge-face and double-layer electrostatic interactions, potentially forming local gel regions in which the local flow is transformed relatively abruptly from viscous to elastic [4.15-4.16]. One can imagine that in these circumstances, very high levels of local shear will be set up in the polyethylene, lowering the free energy barrier for crystallisation. TEM micrographs in Chapter 2 showed that the sub-micron dispersion of intercalated material is finer in the NC20 than NB20. Furthermore, morphological analysis of deformed samples in Chapter 5 evinces highly nonuniform stress fields in NC5 and NC20 that cannot be seen in NB5 and NB20. The effect of shear history on morphology should be investigated, not least because materials with substantial shear memories are not commercially viable if a small uncertainty in the production process can give rise to a large uncertainty in the resulting morphology.

During crystallisation, does the PE move relative to the o-MMT or vice versa? This question cannot be answered decisively from these images. The relative alignment of silicate layers and nylon-6 crystallites following injection moulding has been studied by Kojima *et al.* [4.17] using WAXS and TEM. They found that near the middle of the sample (the low-shear region), the silicate layers were randomly orientated perpendicular to the crystallites. Conversely, in the surface region, both the clay layers and crystallites were oriented parallel to the surface. It was discovered that an intermediate layer existed in which the clay layers and crystallites were perpendicular to and parallel to the surface respectively, implying that polymer-polymer interactions were capable of moving the clay. Of course, because the mutual orthogonality of crystallites and silicate layers of necessity involves the generation of torque, their relative mobility is not directly comparable to the situation in which polyethylene lamellae grow parallel to the platelets. Extensive studies are needed to clarify this question.

Another question that should be considered is that of interactions in the melt prior to crystallisation. The presence of the clay may induce an instability in the free energy of mixing between the LPE and BPE, leading to phase separation in reciprocal space [4.18]. Alternatively, in the metastable case, regions of increased concentration around clay particles can be considered as nucleation and growth processes [4.19].

In the late 1970s, Pechhold proposed that the melt phase may not be completely amorphous [4.20]. He argued that under some conditions it may become thermodynamically favourable for clustering to occur in chain orientation. Groups of aligned chains then undergo coordinated folding, otherwise known as “super-folding,” in order to achieve maximum entropy. More recently, Strobl [4.21] has put forward a hypothesis based on consideration of a wide range of SAXS, TEM, atomic force microscopy, optical microscopy and light scattering experiments found in the literature. He argues that crystallisation generally proceeds via mesomorphic phases of weakly associating chains. Local fusion occurs in this phase, leading to lamellar blocks which eventually form together. This, it is argued, leads to the granular block structure which can be observed experimentally. Whatever the case, it is clear that it would be very useful to conduct experiments on PE-MMT composites both in the melt phase and at very high crystallisation temperatures, where both liquid-liquid and liquid-solid phase transitions operate simultaneously.

The literature offers surprisingly few papers that deal with semicrystalline nanocomposite morphologies in depth; the ones that do exist primarily comprise TEM and SEM studies of particle size distribution [4.22-4.23.] Increases in nucleation density have been observed for various systems [4.24-4.25] along with increases in morphological roughness. In particular, Lamellar roughness in polypropylene / MMT nanocomposites has been observed by polarised optical microscopy and AFM [4.26]. However, the power of detailed morphological characterisation for probing the underlying interactions has simply not been exploited.

4.8 Conclusions

SEM has been used to draw a number of conclusions about the morphological effects of masterbatch chemistry and loading level. The Nanocor systems are temperature dependant, with a critical temperature below which nucleation densities and growth trajectory disorder massively increase. Conversely, the effects of the Nanoblend do not exhibit a temperature threshold, and they do not involve gross morphological disorder. Rather, a lamellar roughening and straightening effect exists even at the lowest loading levels. This leads to banding suppression and to the formation of domains within the superlamellar objects: long-range order is swapped for short-range order. Conversely, crystallisation of NC20 at 117 °C yields long-range order in the form of a highly oriented lamellar structure. A better understanding of these effects could enable versatile morphological design through the fine tuning of clay chemistry, blend composition, shear and thermal history.

The invariance of the lamellar long period on all systems is noteworthy. In these systems, this parameter is much more strongly influenced by polymer-polymer interactions than by polymer-clay interactions. More research is needed to determine whether this situation can be changed with improved clay dispersion at small length scales, or whether it is more viable from a materials design perspective to control this parameter independently through engineering the molecular architecture of the matrix polymer. In this scenario, the nucleation and superlamellar morphologies could be controlled by parameters associated with the clay, with the polymer chemistry determining the lamellar long period. This extra set of variables would be expected to enable the fine tuning of mechanical properties as stresses and strains are distributed through the network of clay particles and lamellae.